

Hubble Space Telescope Observations of [O III] Emission in Nearby QSO2s: Physical Properties of the Ionised Outflows

Anna Trindade Falcão,¹★ S. B. Kraemer,¹ T. C. Fischer,² D. M. Crenshaw,³ M. Revalski,² H. R. Schmitt,⁴ M. Vestergaard,^{5,6} M. Elvis,⁷ C.M. Gaskell,⁸ F. Hamann,⁹ L. C. Ho,¹⁰ J. Hutchings,¹¹ R. Mushotzky,¹² H. Netzer,¹³ T. Storchi-Bergmann,¹⁴ T.J. Turner,¹⁵ M.J. Ward¹⁶

¹*Institute for Astrophysics and Computational Sciences, Department of Physics, The Catholic University of America, Washington, DC 20064, USA*

²*Space Telescope Science Institute, Baltimore, MD 21218, USA*

³*Department of Physics and Astronomy, Georgia State University, Astronomy Offices, 25 Park Place, Suite 600, Atlanta, GA 30303, USA*

⁴*Naval Research Laboratory, Washington, DC 20375, USA*

⁵*Dark Cosmology Centre, Niels Bohr Institute, University of Copenhagen, Jagtvej 128, 2200 Copenhagen N, Denmark*

⁶*Steward Observatory and Department of Astronomy, University of Arizona, 933 N. Cherry Avenue, Tucson AZ 85721*

⁷*Harvard-Smithsonian Center for Astrophysics, 60 Garden St., Cambridge, MA 02138, USA*

⁸*Department of Astronomy and Astrophysics, University of California, Santa Cruz, CA 95064, USA*

⁹*Department of Physics and Astronomy, University of California, Riverside, CA 92507, USA*

¹⁰*Kavli Institute for Astronomy and Astrophysics, Peking University; School of Physics, Department of Astronomy, Peking University; Beijing 100871, China*

¹¹*Dominion Astrophysical Observatory, NRC Herzberg Institute of Astrophysics, 5071 West Saanich Road, Victoria, BC, V9E 2E7, Canada*

¹²*Department of Astronomy, University of Maryland, College Park, MD 20742, USA*

¹³*School of Physics and Astronomy, Tel Aviv University, Tel Aviv 69978, Israel*

¹⁴*Departamento de Astronomia, Universidade Federal do Rio Grande do Sul, IF, CP 15051, 91501-970 Porto Alegre, RS, Brazil*

¹⁵*Department of Physics, University of Maryland Baltimore County, 1000 Hilltop Circle, Baltimore, MD 21250, USA*

¹⁶*Centre for Extragalactic Astronomy, Department of Physics, University of Durham, South Road, Durham DH1 3LE, UK*

Accepted XXX. Received YYY; in original form ZZZ

ABSTRACT

We use Hubble Space Telescope (*HST*)/ Space Telescope Imaging Spectrograph (STIS) long-slit G430M and G750M spectra to analyse the extended [O III] $\lambda 5007$ emission in a sample of twelve nearby ($z < 0.12$) luminous ($L_{\text{bol}} > 1.6 \times 10^{45} \text{ erg s}^{-1}$) QSO2s. The purpose of the study is to determine the properties of the mass outflows of ionised gas and their role in AGN feedback. We measure fluxes and velocities as functions of radial distances. Using Cloudy models and ionising luminosities derived from [O III] $\lambda 5007$, we are able to estimate the densities for the emission-line gas. From these results, we derive masses of [O III]-emitting gas, mass outflow rates, kinetic energies, kinetic luminosities, momenta and momentum flow rates as a function of radial distance for each of the targets. For the sample, masses are several times $10^3 M_{\odot}$ - $10^7 M_{\odot}$ and peak outflow rates are $9.3 \times 10^{-3} M_{\odot} \text{ yr}^{-1}$ to $10.3 M_{\odot} \text{ yr}^{-1}$. The peak kinetic luminosities are 3.4×10^{-8} to 4.9×10^{-4} of the bolometric luminosity, which does not approach the 5.0×10^{-3} - 5.0×10^{-2} range required by some models for efficient feedback. For Mrk 34, which has the largest kinetic luminosity of our sample, in order to produce efficient feedback there would have to be 10 times more [O III]-emitting gas than we detected at its position of maximum kinetic luminosity. Three targets show extended [O III] emission, but compact outflow regions. This may be due to different mass profiles or different evolutionary histories.

Key words: galaxies: active – galaxies: QSO2 – galaxies: kinematics and dynamics

1 INTRODUCTION

An Active Galactic Nucleus (AGN) is a compact region at the centre of a galaxy that emits a significant amount of energy over much of the electromagnetic spectrum, and whose spectral characteristics indicate that the energy source is non-stellar. Such objects have been observed in the infrared, X-ray, radio, microwave, gamma-ray and optical/ultraviolet wavebands.

Accreting supermassive black holes (SMBHs) are believed to be

the central engines that power all AGN. This accretion is the result of mass inflows to the central SMBH that can be triggered both from outside the galaxy, via interactions with companions, or from inside it, via secular processes (Storchi-Bergmann & Schnorr-Muller 2019). The generally adopted picture is that of a small continuum source, associated with the mass accretion flow that feeds the SMBH, surrounded by a much larger emission-line region (Osterbrock & Ferland 2006; Crenshaw et al. 2010; Kraemer et al. 2012). The extended (10s - 1000s of pc) ionised gas in AGN is referred to as the "Narrow Line Region"(NLR). Here the typical electron density is 10^2 - 10^6 cm^{-3} (Peterson 1997), and the gas velocity is 300-1100 km s^{-1} . The

★ E-mail: anna.trindade04@gmail.com

radiation released by the accretion flow to the SMBH can interact with the interstellar stellar medium of the host galaxy, ionising and accelerating the gas. This process may regulate the SMBH accretion rate. The relationship between the SMBH mass and the stellar velocity dispersion of its galaxy bulge (Kormendy & Ho 2013, and references therein) is credited to the action of the AGN quenching star formation and evacuating gas from the bulge, a process referred to as "AGN feedback" (Begelman 2004).

Various physical scenarios for effective feedback have been suggested. These include quenching star formation through negative feedback (Wylezalek & Zakamska 2016), triggering star formation through positive feedback (Silk 2013; Mahoro et al. 2017) or more complex interactions (Zubovas & Bourne 2017).

AGN feedback certainly exists in radio loud AGNs, whose powerful jets are highly collimated, but they occur in only 5-10% of the AGN population (Raftar et al. 2009). Meanwhile, winds are prevalent in most AGN (Mullaney et al. 2013; Genzel et al. 2014; Woo et al. 2016). AGN winds are frequently observed as UV and X-ray absorption lines blueshifted with respect to their host galaxies, originating in gas within tens to hundreds of parsecs from the central SMBH (Crenshaw et al. 2003; Veilleux et al. 2005; Crenshaw & Kraemer 2012; King & Pounds 2015), or emission-line gas in AGN narrow-line regions (Crenshaw & Kraemer 2005; Crenshaw et al. 2010; Müller-Sánchez et al. 2011; Fischer et al. 2013, 2014; Bae & Woo 2016; Nevin et al. 2016). Recent studies (e.g., Fischer et al. 2018, hereafter F2018) question how effective AGN feedback is on galactic-bulge scales, as required in a star-formation quenching, negative feedback scenario. Therefore it is important to quantify its impact, which can be accomplished by characterising the physical properties of these outflows, such as mass, velocity, mass outflow rate, and kinetic energy.

While previous studies suggested that the power of the outflows scale with luminosity (Ganguly & Brotherton 2008), some ground-based studies of QSO2s (Greene et al. 2011; Liu et al. 2013; Harrison et al. 2014; McElroy et al. 2015) have found that powerful and very extended outflows detected by the optical [O III] $\lambda 5007$ emission line are extremely rare. This raises the question of whether kpc-scale AGN winds exist in most QSO2s. The answer to this question can be decisive on the matter of whether outflows are a critical component of quasars feedback and hence the evolution of galaxy bulges, or if the star formation is quenched in bulges by other means.

F2018 obtained *HST* imaging and spectroscopy of 12 of the 15 most luminous targets at $z \leq 0.12$ from the Reyes et al. (2008) sample of QSO2s, through Hubble Program ID 13728 (PI: Kraemer) and archival observations of Mrk 34 (see Table 1). They measured [O III] velocities and line profile widths as a function of radial distance in order to characterise mass outflows in these QSO2s.

In regard to the morphology of the sample, F2018 found that in some of the targets the [O III] region is very extended, such as in FIRST J120041.4+314745, which has a maximum radial extent in its [O III] image, R_{max} , of 5.92 kpc. Meanwhile, other targets present a very compact morphology, such as 2MASX J14054117+4026326 which possesses a $R_{max} = 0.88$ kpc.

Regarding the kinematics of the ionised gas, F2018 showed that the extent of the outflows, R_{out} , in most of the sample, is relatively small compared to the overall extent of the [O III] emission region, R_{max} , with an average $R_{out}/R_{max} = 0.22$, except for Mrk 34, for which $R_{out}/R_{max} \sim 1$ (see Table 1). They found that one can categorize the influence of the central AGNs in different regions, as a function of distance from the nucleus. In the inner region, the emission lines have multiple components and include velocity profiles that differ from rotation, i.e., with high central velocities and high

Full Width at Half Maximum (FWHM), and hence are consistent with outflows. At greater distances, gas is still being ionised by the AGN radiation but emission lines exhibit low central velocities with low FWHM, consistent with rotation of the host galaxy. In addition, F2018 identified a third kinematic component, namely, gas with low central velocities, but high FWHM. They refer to this as "disturbed" kinematics and suggested that AGN activity may be disrupting gas without resulting in radial acceleration.

Previous work (Fischer et al. 2017; Wylezalek & Morganti 2018) explored the idea that the outflows are radiatively accelerated, although we see in our targets a rotational component as well. At large distances, this is consistent with the fact that the flux of radiation is low, but the gravitational deceleration due to the enclosed stellar mass is large, therefore the gas cannot be radially accelerated. However, at smaller distances, the rotation component may simply be gas that has not been exposed to the AGN radiation long enough to be accelerated.

In this study, we use the same data as F2018, and we extend their analysis by computing masses, mass outflow rates, kinetic energies, kinetic energy rates, momenta and momentum flow rates for the same sample of QSO2s. Throughout this paper we adopt a flat Λ CDM cosmology with $H_0 = 71 \text{ km s}^{-1} \text{ Mpc}^{-1}$, $\Omega_0 = 0.28$ and $\Omega_\Lambda = 0.72$.

2 SAMPLE, OBSERVATIONS AND MEASUREMENTS

2.1 *HST* Observations

We use medium dispersion spectra¹ to characterise the physical properties and kinematics of the emission-line gas, along with [O III] imaging to determine the ionised gas mass. As already discussed in F2018, the observing program for our sample was performed in a two-step process: first, we obtained narrow-band images of each AGN to determine ideal STIS position angles and, later, a spectroscopic observation. To obtain the images for our sample, FR505N or FR551N filters were used, chosen depending on the redshift of each target to observe [O III], with the Wide-Field Channel (WFC) of *HST*/Advanced Camera for Surveys (ACS). The FR647M filter was used to obtain the continuum observations.

The long slit spectra used in this study were obtained with STIS using either the G430M or G750M gratings to study the [O III] kinematics, employing a $52'' \times 0.2''$ slit oriented along the major axis of the NLR.

2.2 Spectral Fitting

We fit the emission line in each row (i.e., in the spatial direction) of the STIS spectral image with Gaussians in order to obtain the [O III] velocities, relative to systemic, and fluxes. We employ a Bayesian fitting routine, discussed by Fischer et al. (2017), that uses the Importance Nested Sampling algorithm in the MultiNest library (Feroz & Hobson 2008; Feroz et al. 2009, 2013; Buchner et al. 2014) to compute the logarithm of the evidence, $\ln(Z)$, for each model, as shown in Figure 1.

The models are run for zero Gaussian components, i.e., no [O III] emission, and then for one Gaussian component. If the one-component model is chosen over the zero component model² the data are analysed with a two-component model, and the process is

¹ $R = \lambda/\Delta\lambda \sim 5000\text{--}10,000$ (Woodgate et al. 1998)

² The one component model has to have a significantly better evidence value, $|\ln \frac{Z_1}{Z_0}| > 5$, in order to be chosen over the zero component model.

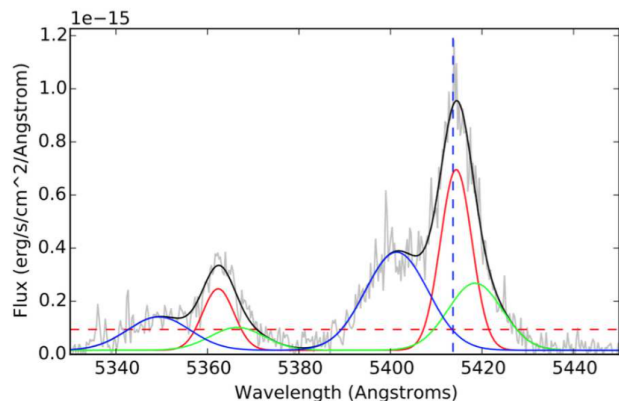


Figure 1. [O III] $\lambda 4959, \lambda 5007$ emission-line component fitting example over the continuum peak in 2MASX J08025293+2552551. The continuum peak refers to the brightest row in the 2D CCD data, where, if one takes a vertical, 1D cut along the image (avoiding the emission lines), that row would be the peak of the flux distribution. [O III] $\lambda 4959$ fit parameters are fixed to be identical to [O III] $\lambda 5007$ fit parameters, with line flux fixed to be 1/3 of [O III] $\lambda 5007$ flux. Grey line represents STIS spectral data. Solid black line represents the total model. Red, blue, and cyan lines represent individual Gaussians. Vertical dashed blue line represents the [O III] $\lambda 5007$ wavelength at systemic velocity. Horizontal dashed red line represents the 3σ continuum-flux lower limit for Gaussians in our fitting. Figure from Fischer et al. 2018.

repeated until the more complex model ($\ln Z_{n+1}$) is no longer chosen over the previous one ($\ln Z_n$). The uncertainty in flux for each line is calculated from the residuals between the data and the fit. However, the flux uncertainties are small compared to those discussed in section 2.4.

2.3 [O III] Image Analysis

In order to account for the mass of [O III] emitting gas outside of the area sampled by the STIS slit, we use a continuum-subtracted [O III] emission line image of the entire NLR for each target. The flux calibration included scaling by the filter bandpass. These correction factors are equal to 2% of the linear ramp filter wavelength, or approximately 100 Å, for each image (Ryon 2019).

Our measurements and velocities discussed in section 2.2 are deprojected according to the analysis of the Sloan Digital Sky Survey (SDSS) images, as described in F2018. An example of the [O III] image and azimuthally summed flux profile are shown in Figure 2, for FIRST J120041.4+314745.

To determine the total [O III] flux as a function of distance from the nucleus, we use the Elliptical Panda routine, in the SAOImage DS9 Software (Joye & Mandel 2003). Following F2018 (see sections 2.5 and 3.1 of F2018), we assume that the host galaxies are disc galaxies and that the inclination of their discs to our line of sight can be obtained from the ellipticities of their isophotes. The ellipticities and position angles (PAs) of our targets are given in Table 2 of F2018 along with the PAs of the ionization cones. Following Fischer et al. (2017) and F2018, we furthermore assume that most of the AGN-ionized gas structure in type-2 AGNs lies in their host disks, and that we can thus use the host disc orientation assumed for each galaxy to deproject *HST* measurements for our QSO2 sample to determine true physical distances in the plane of the host galaxy. Annuli of constant distance from the centres of the galaxies are ellipses with their major

axes in the PA as given in Table 2 of F2018. We add up the [O III] flux in a series of elliptical annuli of radius δr (see Table 1), where δr is the deprojected length along the slit for each extraction. These annuli are illustrated for one of our targets in the left-hand panel of Figure 2. We divide each elliptical annulus in two with one half for each side of the ionization cone.

2.4 Constraints on Luminosity

In Type 2 AGNs, the inner region, nearest to the SMBH, is hidden from view (Antonucci 1993), therefore one has to use indirect indicators to estimate the bolometric luminosity, except in cases where the X-ray absorber is not Compton-thick. One method is to use the total [O III] luminosity, $L_{[O III]}$, and a bolometric correction factor (e.g., Heckman et al. 2004), but there is some uncertainty in the value of the factor depending on the extinction (Lamastra et al. 2009) and the Eddington ratio (Duras et al. 2020).

In order to estimate the extinction towards the NLRs of the QSO2s, we retrieved the fluxes of $H\alpha$ and $H\beta$ from SDSS (Ahumada et al. 2019). The observed ratios of $H\alpha/H\beta$ range from 4.7, for 2MASX J07594101+5050245, to 3.5, for FIRST J120041.4+314745. In AGN, the intrinsic ratio can range from the theoretical ratio, 2.9 (Osterbrock & Ferland 2006), to ~ 3.1 , for broad-line decrements (Dong et al. 2008). Since our sample consists of QSO2s, we are only detecting Balmer lines from the NLR, therefore, to calculate the reddening, we assume an intrinsic ratio of 3.0. Taking into account this intrinsic ratio, and the Galactic extinction curve (Savage & Mathis 1979)³, we calculate the reddening, $E(B-V)$, for all the targets in our sample. We assume that the same reddening applies to the entire [O III] emitting regions for each target in our sample. Note that the extinction occurs in dust along our line of sight, both within the Galaxy and the individual QSOs. The results are listed in Table 2.

To calculate the values for the bolometric luminosity, L_{bol} , for our targets, we correct the values of $L_{[O III]}$ as described in Seaton (1979), using the reddening listed in Table 2. Then, we calculate L_{bol} using the corrected $L_{[O III]}$ and the bolometric correction factor from Lamastra et al. (2009), which is 454 for the range in luminosities in our sample⁴. Our results are listed in Table 2.

For the entire Spectral Energy Distribution (SED), we assume that it can be fitted using a number of broken power-laws of the form:

$$L_\nu \propto \nu^{-\alpha} \quad (1)$$

where α , the spectral or energy index, is a positive number (e.g., Laor et al. 1997; Meléndez et al. 2011). We assume that the UV to lower energy, “soft” X-ray, is characterised by one value of α , while the higher energy, “hard” X-ray, has a lower value of α . For our study we adopt a cutoff at 100 keV and we set the breakpoint at 500 eV, using the following values (Revalski et al. 2018):

$$\begin{aligned} \alpha &= 1.0 \text{ for } h\nu < 13.6 \text{ eV;} \\ \alpha &= 1.4 \text{ for } 13.6 \text{ eV} \leq h\nu \leq 500 \text{ eV;} \\ \alpha &= 1.0 \text{ for } 500 \text{ eV} \leq h\nu \leq 10 \text{ keV;} \end{aligned}$$

³ Using the extinction curve of Cardelli et al. (1989), results in a less than 4% change in the computed reddening, compared to the curve of Savage & Mathis (1979).

⁴ There are other ways to calculate the bolometric luminosity using the combined [O III]+[O I] or $H\beta$ and [O III], as described in Netzer (2009). Based on the SSD spectra, using these methods, we obtain $L_{bol} = 1.4 \times 10^{45}$ erg s⁻¹ for Mrk 34, which is in reasonable agreement with what we obtain using the corrected [O III] and the Lamastra correction for this target.

$\alpha = 0.5$ for $10 \text{ keV} \leq h\nu \leq 100 \text{ keV}$;

It is likely that the "soft" X-ray continuum is more complex than what we assume (e.g., [Netzer et al. 2002](#); [Kraemer et al. 2002](#)). However, we opt to use the same SED as in [Revalski et al. \(2018\)](#) to allow for a direct comparison of the results for Mrk 34.

The number of ionising photons per second emitted by the AGN, based on this SED, is:

$$Q = C_2 \int_{13.6 \text{ eV}}^{500 \text{ eV}} \left(\frac{\nu^{-1.4}}{h\nu} \right) d\nu + C_1 \int_{500 \text{ eV}}^{10 \text{ keV}} \left(\frac{\nu^{-1.0}}{h\nu} \right) d\nu + C \int_{10 \text{ keV}}^{100 \text{ keV}} \left(\frac{\nu^{-0.5}}{h\nu} \right) d\nu \quad (2)$$

where h is the Planck constant.

Specifically for Mrk 34, [Gandhi et al. \(2014\)](#) were able to determine the X-ray luminosity, $L_{(2-10 \text{ keV})} = 9(\pm 3) \times 10^{43} \text{ erg.s}^{-1}$, which makes it possible to calculate Q for this target. They did not detect any significant variability between their *NuSTAR* and *XMM-Newton* observations. Therefore, we do not consider the possible variability of the X-ray source. The constants C , C_1 and C_2 were determined by normalizing to the $L_{(2-10 \text{ keV})}$.

We then use the corrected $L_{[\text{O III}]}$ for Mrk 34 to get the ratio $Q/L_{[\text{O III}]}$, which we apply to all the other QSO2s. Our results are presented in Table 2.

In order to estimate the uncertainties introduced by our SED, we recalculate Q for $1.0 \leq \alpha \leq 1.8$, over the range from 13.6 eV to 500 eV. This results in a factor of 3 change compared to the value of Q computed for $\alpha = 1.4$. Other sources of uncertainty include those of: the X-ray luminosity, which [Gandhi et al.](#) assumed to be $\sim 30\%$; the uncertainty in the ratio $H\alpha/H\beta$, $\sim 15\%$; a factor of 2 in our assumed ionization parameter; the deprojected positions, $\sim 10\%$; and a factor of 2 uncertainty in the correction for the bolometric luminosity ([Lamastra et al. 2009](#)). Adding all these in quadrature, results in an uncertainty of a factor of ~ 4 , which applies to the hydrogen density determination (see section 2.5).

We also can compare the value for L_{bol} for Mrk 34 derived from the corrected [O III] with the value computed from our model SED. The latter method consists of extending the SED down to 1 eV and, using $\alpha = 1.0$ from 1 eV to 13.6 eV, calculating the bolometric luminosity by integrating over the continuum. The value we get for L_{bol} from our SED is $\sim 58\%$ of the [O III] derived value. The difference could be due to our assumed SED or the reddening correction applied to the [O III] emission. However, the difference is less than the uncertainties in Q discussed in the previous paragraph.

2.5 Photoionisation Models and Constraints on Gas Density

To convert observed [O III] fluxes in a slit element into masses of gas at that position we need to know the volume of emitting gas and its density. This is conventionally done by using density-sensitive line ratios such as the [S II] and [O II] doublet ratios. Since we only have observations of [O III] (and $H\beta$ for three of the targets in our sample, as discussed in section 2.4), we estimate the density from the dimensionless ionization parameter, U , where:

$$U = \frac{Q}{4\pi r^2 n_H c} \quad (3)$$

where r is the radial distance from the AGN, n_H is the hydrogen number density (see section 2.4) and c is the speed of light. We compute the values of $Q(H)$ for all the QSO2s in the sample, as shown in Table 2.

[Revalski et al. \(2018\)](#) used a multi-component photoionisation model for Mrk 34. Based on the model parameters and results given

in their Tables 6 and 7, the "medium" component, for which they assumed $\log(U) = -2$, accounts for most the [O III] emission. Also, this component contains almost all the mass at each of the points modelled by them, except for 2 positions, where the ionisation is dominated by a higher ionisation component. This results in their determination of higher densities for the [O III] component, as shown in Figure 3. Therefore we model the [O III] emission-line gas, at each radial position, with a single component of $\log(U) = -2$. This means that the density drops with r^{-2} , for the [O III] gas along the whole emitting region (as also proposed by [Davies et al. 2020](#)).

We use version 17.00 of Cloudy ([Ferland et al. 2017](#)) to construct photoionisation models with $\log(U) = -2$. These predict $\frac{[\text{O III}]}{H\beta} \geq 10$, which we confirmed for the targets with both [O III] and $H\beta$ based on measurements of the STIS spectra (2MASX J07594101+5050245, 2MASX J11001238+0846157 and 2MASX J16531506+2349431, which have an average $\frac{[\text{O III}]}{H\beta} = 10.2$).

In dusty gas, emission lines are suppressed by two mechanisms. One is the dust absorption of multiply scattered resonance lines, such as Ly- α (e.g., [Kraemer & Harrington 1986](#)). The other is due to the depletion of elements, such as Si, Mg, and Fe onto dust grains. STIS long-slit UV spectra of the NLR typically show fairly strong Mg II $\lambda 2800$ ([Kraemer et al. 2000, 2001](#); [Collins et al. 2005](#)), which suggests that the refractory elements are not heavily depleted. While these spectra reveal a wide range of Ly- α / $H\beta$ ratios, they generally range from 10 - 20, which indicates the presence of some dust within the emission-line gas. Based on these studies, we assume a dust-to-gas ratio of 50% that of the Galactic interstellar medium with proportional depletion of elements from gas phase, consistent with [Revalski et al. \(2018\)](#). This dust is not the source of the line of sight reddening discussed in section 2.4.

While super-solar abundances appear to be common in broad line region gas, at least in QSOs (e.g., [Hamann & Ferland 1998](#); [Dietrich et al. 2003](#)), NLR studies indicate abundances closer to solar ([Nagao et al. 2001, 2002](#)). Based on their photoionisation analysis of the NLR, [Groves et al. \(2004\)](#) argued for a N/H ratio approximately twice solar, consistent with other NLR studies (e.g., [Storchi-Bergmann et al. 1996, 1998](#); [Kraemer et al. 1998](#)). Since N/H increases as $(Z/Z_{\text{solar}})^2$ ([Talbot & Arnett 1973](#)), where Z is the fractional abundance of heavy elements, this ratio corresponds to elemental abundances of approximately 1.4x solar, which we adopt for this study.

The exact logarithmic values relative to hydrogen by number are: C = -3.54, N = -3.88, O = -3.205, Ne = -3.92, Na = -5.61, Mg = -4.47, Al = -5.70, Si = -4.64, P = -6.44, S = -4.73, Ar = -5.45, Ca = -5.81, Fe = -4.65, Ni = -5.93. In order to account for the grain composition, we include depletions from gas phase for C, O and the refractory elements (e.g., [Snow & Witt 1996](#)). Note that dust can play an important role in the dynamics of outflows (e.g., [Baron & Netzer 2019](#)). We will be examining the outflow dynamics in our subsequent paper (Trindade Falcão et al. in preparation).

For reference, we calculate the maximum possible column density of the gas emitting [O III]. This is when the gas is radiation bounded. Specifically, the modelling integration stopped when the electron temperature drops below 4000K, at which point the ionising radiation has essentially been exhausted. It is possible that the total column densities are greater than this, but we have no means of detecting that gas in these data. On the other hand, it is quite likely that the gas is not radiation bounded in places. What matters is the volume of gas emitting [O III]. We calculate this in the next section.

As shown in Figure 3, this method does a reasonable job in matching densities from detailed photoionisation models. We then use the

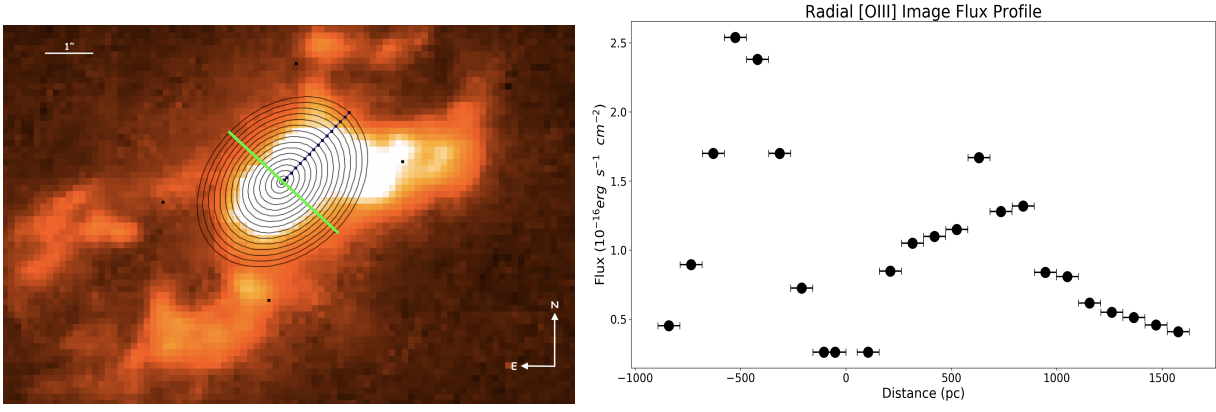


Figure 2. The left panel shows the *HST* [O III] image of FIRST J120041.4+314745 with superimposed elliptical semi-annuli representing rings of constant distance from the nucleus. The green line represents the positions where we divide the two semi-ellipses. The orthogonal black line represents the direction of the slit. The right panel is the [O III] annuli fluxes oriented along the major axis of the ellipse. The negative values are to the southeast and the positive values are to the northwest. Ellipses very close to the nucleus have a very small size, leading to low fluxes in the centre positions. Fluxes at positions > 900 pc (to the southeast side) are too low to be detected. The radial axes in the right panel are asymmetric because the kinematic fits were limited to this range.

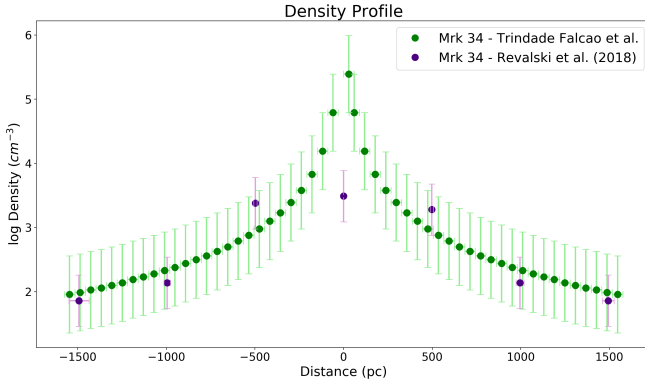


Figure 3. A comparison between the gas densities obtained applying our photoionisation models (in green) and the gas densities obtained by Revalski et al. (2018) (in purple) for Mrk 34. The points in purple are the densities for Revalski et al.'s medium component. Their point at the centre sums up a region ~ 10 times larger than the region we are sampling. Therefore their density is an average over the sampled region, hence much lower than our computed value.

computed column densities, N_H , to calculate the masses and, subsequently, the other physical properties of the [O III] gas, as described in section 4.

3 CALCULATIONS

To determine the various quantities associated with the outflow as a function of distance from the SMBH we first need to determine the mass of gas in each of our semi-annuli. We do this by first estimating M_{slit} , the mass of gas inside the *HST* STIS slit at a given radius, and then scaling this to the mass in the whole semi-annulus by multiplying the ratio of the total [O III] flux in the semi-annulus, $F_{[O III]_{ann}}$, to the flux in the slit, $F_{[O III]_m}$. For our calculations we only consider points lying inside the range of outflow defined in F2018.

The mass of gas emitting [O III], in grams, in each position along the slit is giving by (Crenshaw et al. 2015):

$$M_{slit}(r) = N_H \mu m_p \left(\frac{L_{[O III]}}{F_{[O III]_c}} \right) \quad (4)$$

where N_H is the hydrogen column density, assumed to be the same as the column density modelled by Cloudy, μ is the mean mass per proton⁵, m_p is the mass of a proton. To get the mass of gas the column density needs to be multiplied by an effective area. The term in parentheses gives the effective surface area of the emitting gas as seen by the observer. $F_{[O III]_c}$ is the [O III] luminosity per cm^2 calculated by Cloudy and $L_{[O III]}$ is the observed luminosity calculated from the reddening corrected flux in the slit. That is,

$$L_{[O III]} = 4\pi D^2 F_{[O III]_m} \quad (5)$$

where D is the distance to the QSO2s (see Table 1) and $F_{[O III]_m}$ is the intrinsic flux measure at each point in the STIS spectra.

Physically, the equation for M_{slit} (Equation 4) determines the area of the emitting clouds through the ratio of the luminosity and flux, and then multiplies this by the column density to yield the total number of particles, which, when multiplied by the mean mass per particle, gives the total ionised mass.

We estimate the mass of gas in the half annulus at a given radial distance from the centre by scaling the mass in the slit (Equation 4) by the ratio of the flux in the entire semi-annulus to the flux in the slit.

Specifically, the total ionised mass in outflow at each radial distance is:

$$M_{out}(r) = M_{slit}(r) \left(\frac{F_{[O III]_{ann}}}{F_{[O III]_m}} \right) \quad (6)$$

where $F_{[O III]_{ann}}$ is the flux in each half image annuli of width δr , as shown in Figure 2. Thus, our method assumes that throughout

⁵ We use $\mu = 1.4$, which is consistent with roughly solar abundances.

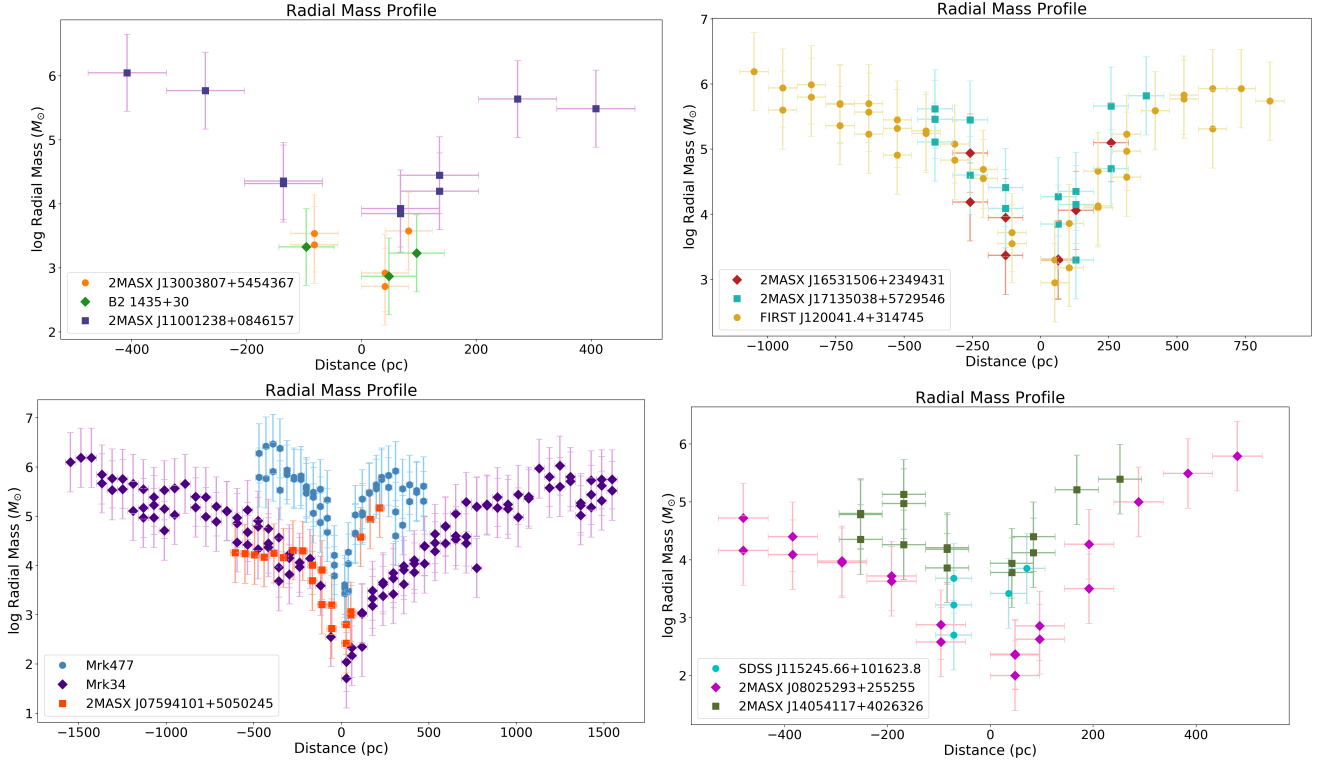


Figure 4. Ionised mass profile in units of M_{\odot} calculated from the total flux in each semi-elliptical annulus for all the targets in our sample. QSO2s with similar redshifts were plotted together. All points considered in the plots are inside the range of outflow defined in Fischer et al. 2018. With a few exceptions, most mass profiles look similar. So the total outflow mass is primarily determined by where the outflow stops and the rotation kinematics begin. Each annulus has a $\delta r = 0.05$ arcsec, and, due to the range in distances of our targets, δr corresponds to a range of physical lengths in pc.

the semi-annulus the gas has the same density, N_H , and outflow velocity, v_{out} , as the gas at the slit location.

After calculating $\dot{M}_{out}(r)$, we are able to estimate the mass outflow rates ($\dot{M}_{out}(r)$), kinetic energies (E), kinetic luminosities (\dot{E}), momenta (p) and momentum flow rates (\dot{p}). All these quantities are related to the power and impact of the NLR outflows (King & Pounds 2015).

The mass outflow rates ($\dot{M}_{out}(r)$) are calculated, at each point along the NLR, using:

$$\dot{M}_{out}(r) = \frac{M_{out}(r)v_{out}}{\delta r} \quad (7)$$

where v_{out} is the deprojected outflow velocity at the distance of the semi-annulus; the deprojection factors are the same as those used in F2018 (see section 2.3).

The kinetic energies (in ergs), kinetic luminosities (in erg/s), momenta (in dyne-s) and momentum flow rates (in dyne⁶) are given by:

$$E(r) = \frac{1}{2} \dot{M}_{out} v_{out}^2 \quad (8)$$

$$\dot{E}(r) = \frac{1}{2} \dot{\dot{M}}_{out} v_{out}^2 \quad (9)$$

$$p(r) = \dot{M}_{out} v_{out} \quad (10)$$

⁶ 1 dyne = 1 g cm s⁻² = 10⁻⁵ N

$$\dot{p}(r) = \dot{\dot{M}}_{out} v_{out} \quad (11)$$

The momenta and momentum flow rates can be compared to the AGN bolometric luminosity, and the radiation pressure force, $\frac{L}{c}$, to quantify the efficiency of the NLR in converting radiation from the AGN into the radial motion of the outflows (Zubovas & King 2012; Costa et al. 2014).

All the uncertainties discussed in section 2.4, which affect our determination of the hydrogen density, result in corresponding uncertainty in our mass calculations. Hence the quantities computed in Equations 7 - 11 have the same factors of uncertainty.

4 RESULTS

We present our mass profiles, outflow rates and other kinematic properties as functions of distance from the SMBH in Figures 4 through Figure 9. The quantities shown are the values within each bin of length δr . Table 3 gives the total masses outflowing and the maxima of the kinematic properties. Table 4 gives the radii of the peaks in these quantities.

Among the QSO2s in our sample, the outflow has a maximum radial extent that extends from 130 pc to 1,600 pc from the nucleus and contains a total ionised gas mass ranging from $4.6^{+13.8}_{-3.45} \times 10^3 M_{\odot}$ to $3.4^{+10.2}_{-2.55} \times 10^7 M_{\odot}$, in the outflow region (Figure 4). The kinematics at further distances are consistent with disturbance and rotation, but not with outflows, as discussed in F2018.

For all targets in our sample, the total ionised mass at the innermost

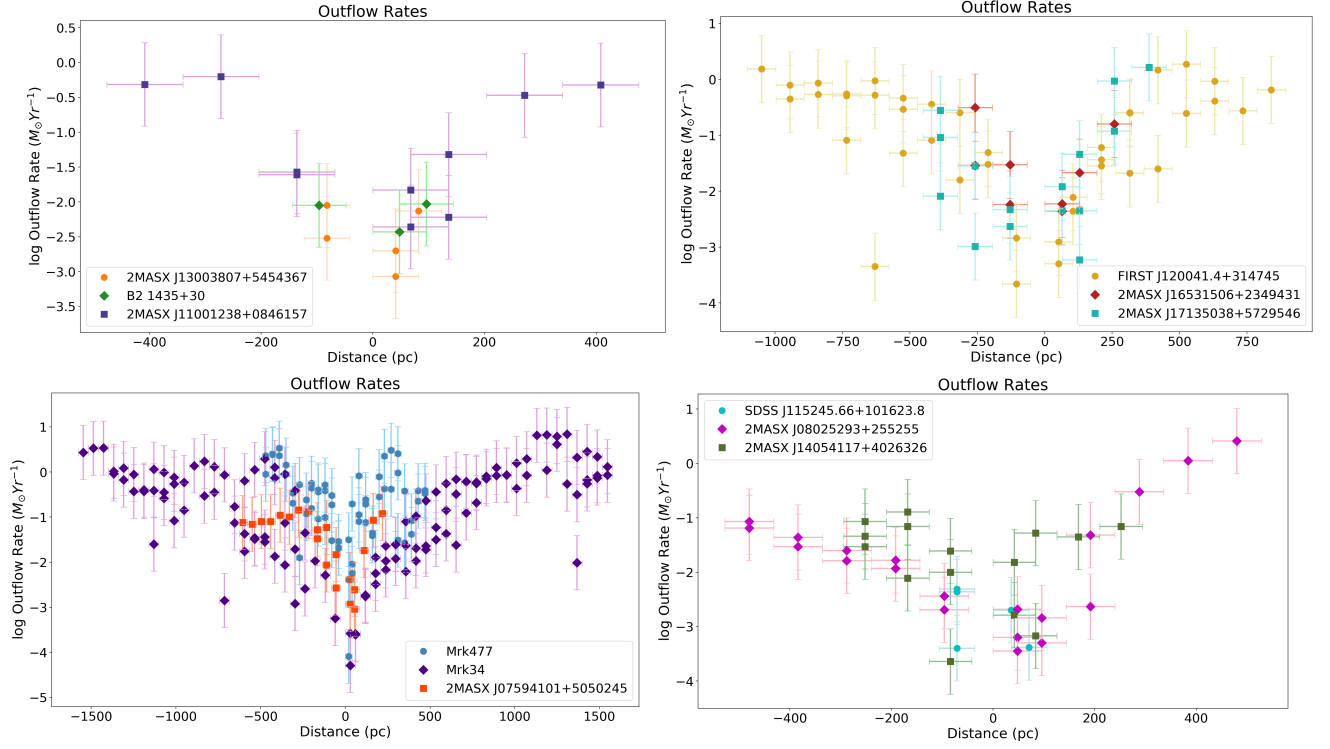


Figure 5. Spatially-resolved outflow rates for all targets, assuming that all of the material is in outflow. Same as Figure 4

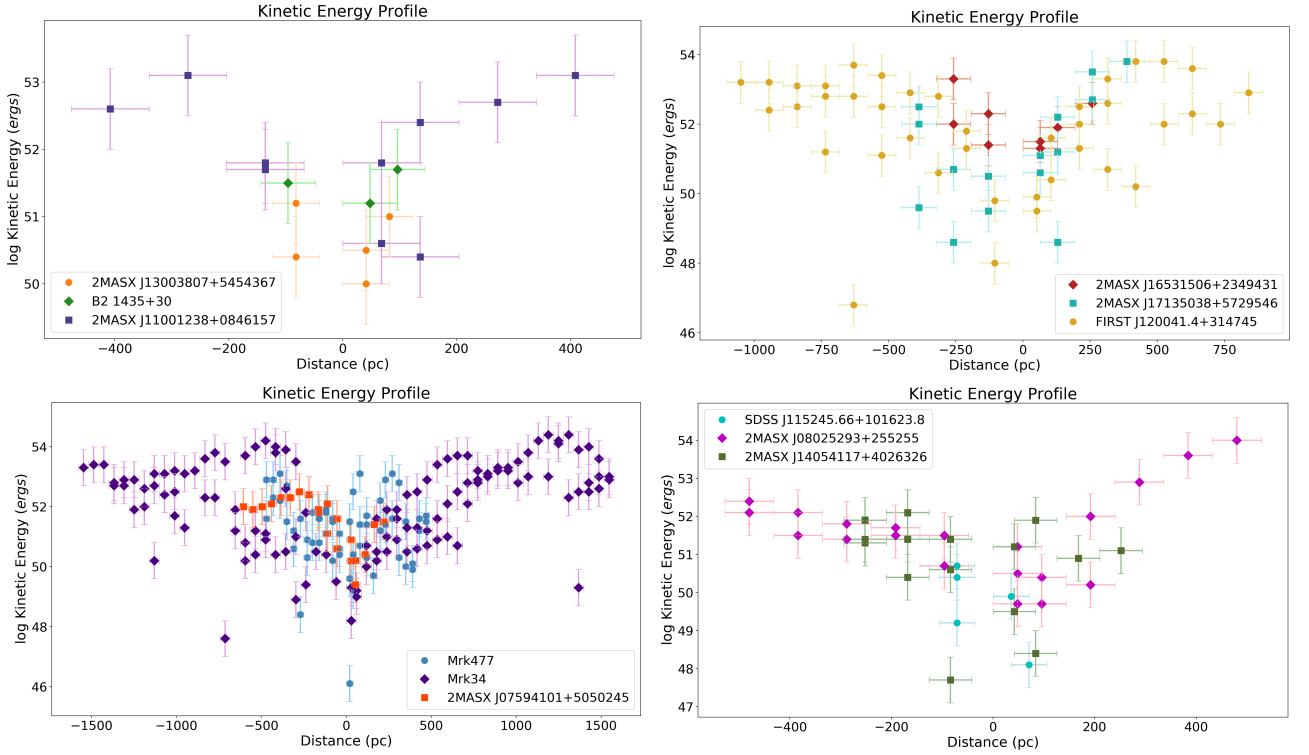


Figure 6. Kinetic Energy profiles for all targets. See section 4.

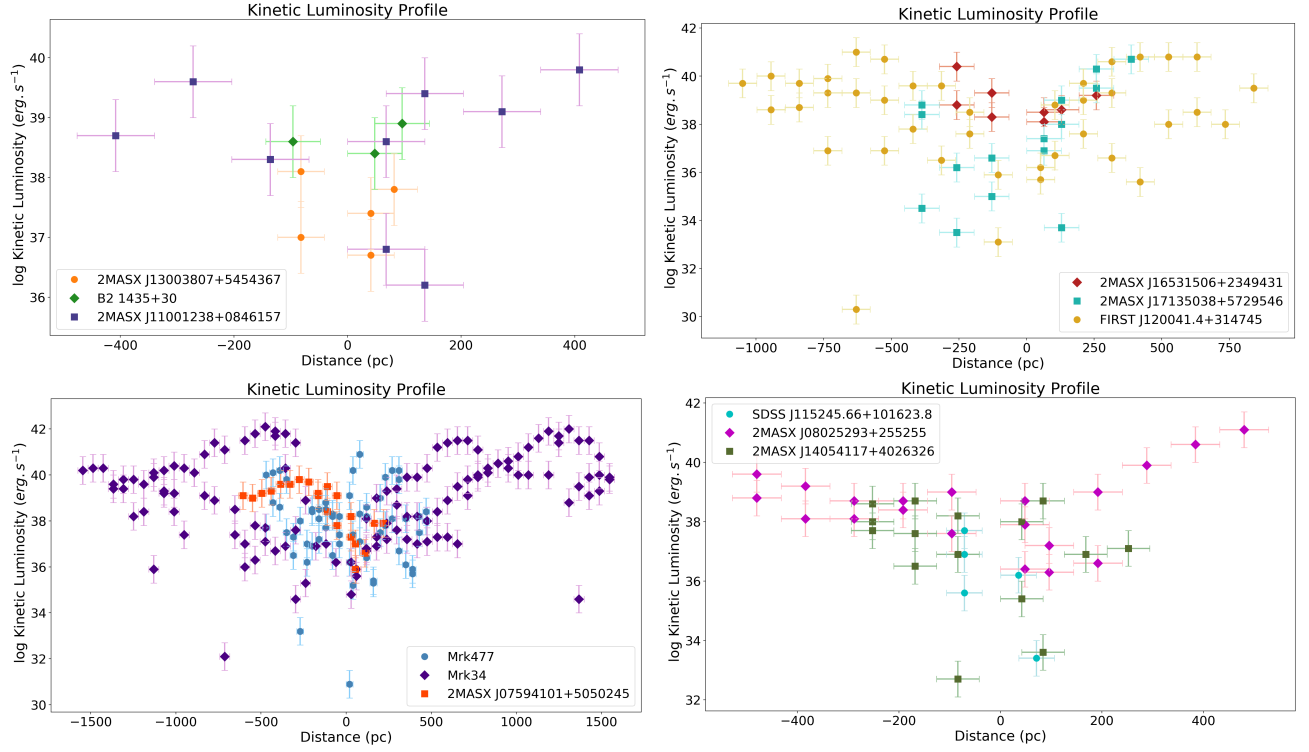


Figure 7. Kinetic Luminosity Rates calculated for all targets. QSOs with similar redshifts were plotted together. See section 4

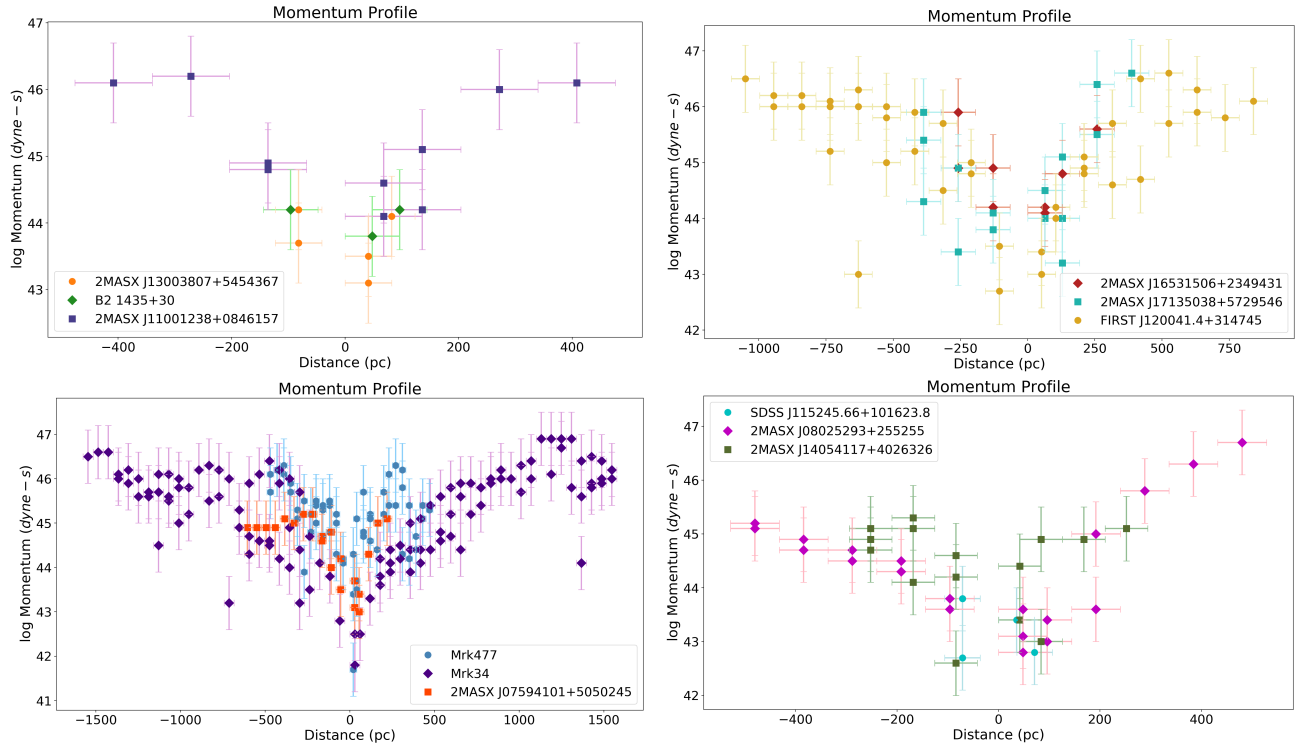


Figure 8. Momentum Profiles for all targets. See section 4

Table 1. Column 4 lists the distance to the QSO2, considering a Hubble constant = $71 \text{ km s}^{-1} \text{ Mpc}^{-1}$. Column 5 lists the maximum radial extent of the AGN driven outflows, with emission lines, which exhibit high centroid velocities and/or multiple emission lines with multiple components. Column 6 lists the maximum radial extent of the disturbed gas, with low centroid velocities and FWHM $> 250 \text{ km s}^{-1}$ (Fischer et al. 2018). Column 7 lists the δr for each target.

Target	Redshift	Scale (kpc $''$)	Distance to QSO2 (Mpc)	Deproj. R_{out} (kpc)	Deproj. R_{dis} (kpc)	δr (pc)
(1)	(2)	(3)	(4)	(5)	(6)	(7)
SDSS J115245.66+101623.8	0.070	1.30	296	0.15	1.23	0.71
MRK 477	0.038	0.72	161	0.54	0.90	0.03
MRK 34	0.051	0.95	215	1.89	1.89	0.06
2MASX J17135038+5729546	0.113	1.97	477	0.65	>0.92	0.13
2MASX J16531506+2349431	0.103	1.83	435	0.57	1.16	0.14
2MASX J14054117+4026326	0.081	1.47	342	0.33	>0.94	0.08
2MASX J13003807+5454367	0.088	1.59	372	0.16	0.16	0.08
2MASX J11001238+0846157	0.101	1.80	427	0.69	>1.51	0.14
2MASX J08025293+2552551	0.081	1.48	342	0.57	0.89	0.09
2MASX J07594101+5050245	0.054	1.02	228	0.67	0.67	0.05
FIRST J120041.4+314745	0.116	2.04	490	1.07	>1.59	0.10
B2 1435+30	0.092	1.66	389	0.20	>1.74	0.09

Table 2. Column 2 lists the corrected [O III] luminosity, as discussed in section 2.4. All targets have $L_{[O III]} \geq 1.9 \times 10^{42}$, satisfying the conventional B-band absolute magnitude criterion of a “quasar”, $B_{mag} < -23$, where a corresponding $L_{[O III]}$ is $> 3 \times 10^8 L_{\odot}$ (Zakamska et al. 2003). Column 3 lists the corrected bolometric luminosity for each QSO2, calculated as described in section 2.4. Column 4 lists the corrected number of ionising photons.s $^{-1}$. Column 5 lists the ratio between the retrieved fluxes of $H\alpha$ and $H\beta$ from SDSS for each target. Column 6 lists the degree of reddening for each target in our sample, calculated using the values for $H\alpha$ and $H\beta$ from their SDSS spectra. Due to the similar redshifts and selection criteria, the range in luminosities is small (by a factor of ~ 4).

Target	$L_{[O III]}$ (erg s $^{-1}$)	L_{bol} (erg s $^{-1}$)	Q (photons s $^{-1}$)	$H\alpha/H\beta$	$E(B-V)$
(1)	(2)	(3)	(4)	(5)	(6)
SDSS J115245.66+101623.8	3.5×10^{42}	1.6×10^{45}	4.8×10^{54}	3.68	0.19
MRK 477	4.0×10^{42}	1.8×10^{45}	5.4×10^{54}	3.76	0.21
MRK 34	5.7×10^{42}	2.6×10^{45}	7.8×10^{54}	3.98	0.26
2MASX J17135038+5729546	6.1×10^{42}	2.8×10^{45}	8.3×10^{54}	3.65	0.18
2MASX J16531506+2349431	1.1×10^{43}	4.9×10^{45}	1.5×10^{55}	4.40	0.35
2MASX J14054117+4026326	4.6×10^{42}	2.1×10^{45}	6.2×10^{54}	4.00	0.26
2MASX J13003807+5454367	4.8×10^{42}	2.2×10^{45}	6.5×10^{54}	3.54	0.15
2MASX J11001238+0846157	8.5×10^{42}	3.9×10^{45}	1.2×10^{55}	3.60	0.17
2MASX J08025293+2552551	8.0×10^{42}	3.6×10^{45}	1.1×10^{55}	4.59	0.39
2MASX J07594101+5050245	8.6×10^{42}	3.9×10^{45}	1.2×10^{55}	4.70	0.41
FIRST J120041.4+314745	1.3×10^{43}	5.8×10^{45}	1.7×10^{55}	3.52	0.15
B2 1435+30	7.1×10^{42}	3.2×10^{45}	9.6×10^{54}	4.33	0.33

points is low (see Figure 4), which can be explained by the fact that the dense gas in this region radiates more efficiently (see Osterbrock & Ferland 2006), leading to smaller masses being required to produce the same observed [O III] emission. Additionally, the area sampled in the annuli is an increasing function of radius, meaning that less mass is added from the images at smaller distances.

The peak in the mass outflow rate peaks from $9.3^{+27.9}_{-7.0} \times 10^{-3} M_{\odot} \text{ yr}^{-1}$, for B2 1435+30, to $10.3^{+30.9}_{-7.7} M_{\odot} \text{ yr}^{-1}$, for Mrk 34 (Figure 5), at a distance varying from 100 pc to 1,260 pc from the nucleus (see Table 4) and then decrease at larger distances.

The maximum kinetic energy for the targets extends from $8.2^{+24.6}_{-6.1} \times 10^{50}$ ergs, for SDSS J115245.66+101623.8, to $2.6^{+7.8}_{-1.9} \times 10^{54}$ ergs, for Mrk 34. The total kinetic luminosity ranges from $3.5^{+10.5}_{-2.6} \times 10^{-8}$ of L_{bol} , for SDSS J115245.66+101623.8, to $4.1^{+12.3}_{-3.1} \times 10^{-3}$ of L_{bol} , for Mrk 34.

The radiation pressure force from the bolometric luminosity, $\frac{L_{bol}}{c}$, ranges from $5.4^{+16.2}_{-4.0} \times 10^{34}$ dyne, for SDSS J115245.66+101623.8, to $1.9^{+5.7}_{-1.4} \times 10^{35}$ dyne, for FIRST J120041.4+314745. The peak momentum flow rate extends from $7.5^{+22.5}_{-5.6} \times 10^{30}$ dyne, for SDSS

J115245.66+101623.8, to $2.8^{+8.4}_{-2.1} \times 10^{34}$ dyne, for Mrk 34. Thus, considering the maximum momentum flow rate among our sample, the peak outflow momentum rate is $\sim 30\%$ of the AGN’s radiation pressure force, although it is a much smaller percentage for most of our sample.

The quantities displayed are the value contained within each bin of width δr . In addition, we neglect contributions to the mass outflow rates and energetics from the significant FWHM of the emission lines, which could be due, for example, to the ablation of gas off the spiral dust lanes.

5 DISCUSSION

The maximum kinetic luminosities of the outflow for our sample are presented in Table 3 and are $(3.4^{+10.2}_{-2.5} \times 10^{-8} - 4.9^{+14.7}_{-3.7} \times 10^{-4})$ of the AGN bolometric luminosities. This does not approach the $5.0 \times 10^{-3} - 5.0 \times 10^{-2}$ range used in models of efficient feedback (Di Matteo et al. 2005; Hopkins & Elvis 2010). The low ratios of \dot{E}/L_{bol} were also found in other samples by Baron & Netzer (2019) and Davies et al. (2020), however, these are much less than those derived from

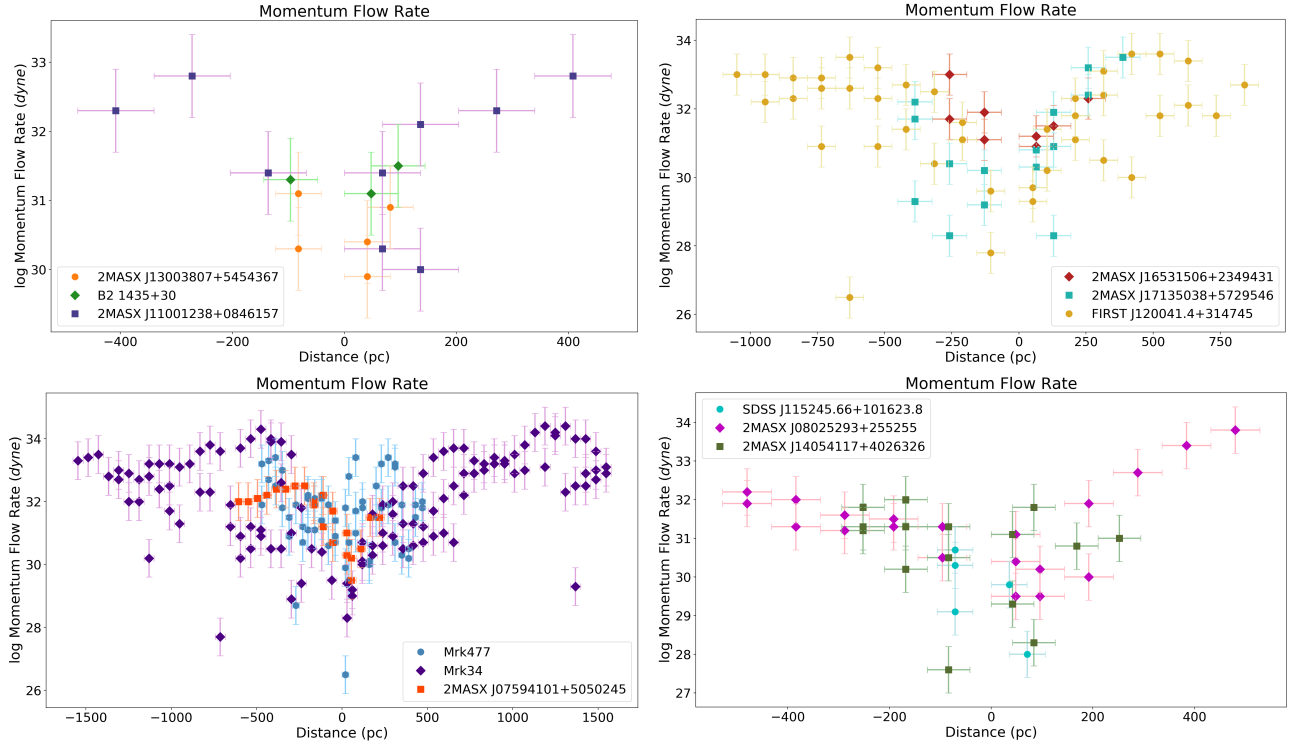


Figure 9. Momentum flow rates. See section 4

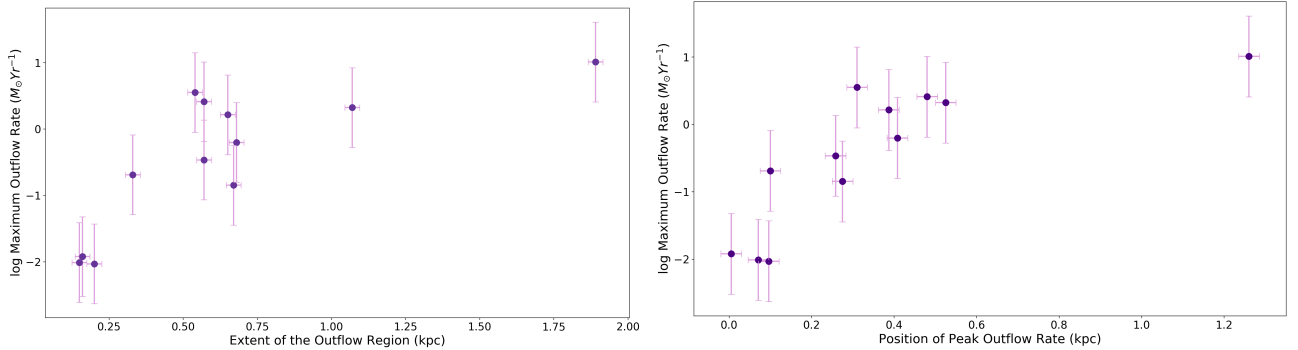


Figure 10. For a majority of our sample, it is possible to see a relation between the maximum outflow rate and R_{out} (left panel) and the position where the peak outflow rate occurs and the maximum outflow rate for each target (right panel).

relativistic outflows (UFOs) observed in the X-ray spectra of some AGN (Bischetti et al. 2019).

We also study the relation between the maximum outflow rate for each target and the position where the maximum outflow rate occurs (Figure 10, right panel), as well as the relation between the maximum outflow rate and R_{out} for each target in our sample (Figure 10, left panel). For a majority of the targets, the maximum outflow rate appears to be correlated with R_{out} , since the further away the gas is from the SMBH, the larger the amount of gas is needed to produce the same amount of ionised gas mass, as the density drops.

After concluding that these QSO2s do not produce effective feedback, based on models previously discussed, we calculate how much mass an outflow would have to have to produce a $\dot{E} = 0.5\%$ of L_{bol} ,

which is considered to be the value where feedback effects could be relevant⁷ (Hopkins & Elvis 2010).

We calculate the required mass for Mrk 34, at its point of maximum \dot{E} , using the highest deprojected outflow velocity component calculated using the fitting routine by Fischer et al. (2017) for that same position, $v_{out} = 1.4 \times 10^3$ km/s. We choose Mrk 34 since, among the targets in our sample, it is the target that shows the highest outflow rate and most extended outflows. We find that, in order to reach the lower limit of $\dot{E}/L_{bol} = 0.5\%$, Mrk 34 would have to possess an outflow rate of $20 M_{\odot} \text{ yr}^{-1}$, in contrast to our measured value of $1.97^{+5.9}_{-1.5} M_{\odot} \text{ yr}^{-1}$. This corresponds to a mass, at that position,

⁷ The maximum \dot{E} does not necessarily occur at the point where the target has its maximum outflow rate, since $\dot{E} \sim v_{out}^3$.

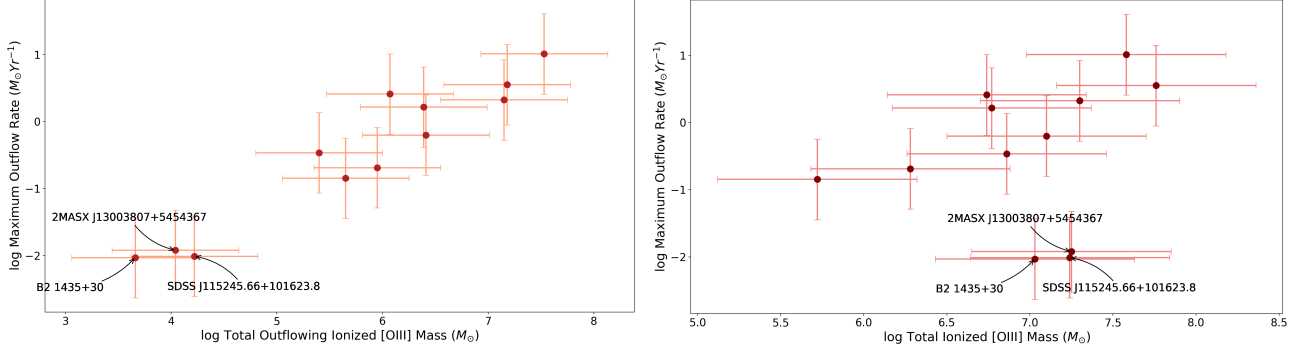


Figure 11. The left panel shows the relation between the maximum outflow rate for each target and the total ionised mass in the outflow range. Right panel shows the relation between the maximum outflow rate for each target and the total ionised mass including the regions outside the outflow range.

of $M_{0.5\%} = 8.2 \times 10^5 M_{\odot}$, as opposed to our measured value of $8.1^{+24.3}_{-6.1} \times 10^4 M_{\odot}$.

We also calculate the maximum amount of mass, M_{max} , that Mrk 34 could have at this distance, i.e., the maximum amount of gas that could be at this distance if the entire solid angle around the SMBH were covered. Specifically:

$$M_{max}(r) = 4\pi r^2 (\mu m_p N_H) \quad (12)$$

where r is the deprojected radial distance. We are assuming the gas is distributed in a complete shell at this distance. We find that the maximum amount of mass that Mrk 34 could possess at this position is $M_{max}(r) = 1.3 \times 10^8 M_{\odot}$, which is greater than the value for $M_{0.5\%}$. However, only a small fraction of that mass is emitting [O III] radiation.

If we consider the position where Mrk 34 has its peak outflow rate, 1.26 kpc, in order to calculate how much mass it would need to reach 0.5% of its bolometric luminosity, and using the highest deprojected outflow velocity at that position, $v_{out} = 6.1 \times 10^2$ km/s, we find that there would need to be an outflow rate of $109 M_{\odot} \text{ yr}^{-1}$, in contrast to our measured value of $4.1^{+12.3}_{-3.1} M_{\odot} \text{ yr}^{-1}$ (in Revalski et al. 2018 the peak outflow rate occurs at ~ 0.5 kpc, where the deprojected outflow velocity is $\sim 2,000$ km/s, which would require an outflow rate of $\sim 40 M_{\odot} \text{ yr}^{-1}$). This corresponds to a mass, at that position, of $1.0 \times 10^7 M_{\odot}$, as opposed to our measured value of $4.0^{+12.0}_{-3.0} \times 10^5 M_{\odot}$. We find that the maximum amount of mass that Mrk 34 could possess at this position is $M_{max}(r) = 7.4 \times 10^8 M_{\odot}$, which is also greater than the value for $M_{0.5\%}$.

These results tell us that the required amount of gas for efficient feedback is less than what we would estimate for a covering factor of unity, which means that it is theoretically possible to have an $\dot{E} = 0.5\%$ of L_{bol} . One explanation for the low values we are obtaining for the mass outflow rate is that the source of the outflow, e.g., cold molecular and possibly atomic gas in the disk (Fischer et al. 2017), has a very low covering factor compared to a sphere at its location.

Another possibility is that the gas does not remain in the state in which it emits [O III] for long. If it is not confined by an external medium, e.g., a lane of gas and dust in the host disk, it will rapidly thermally expand. As it does so, the density drops, and the ionisation state of the gas increases to the point where it becomes X-ray emission line gas (as suggested by Kraemer et al. 2020). In this case, the outflows could be dominated by the X-ray emitting gas. We will be exploring this scenario in a future paper (Trindade Falcão et al. in preparation).

Another characteristic of these targets is the relation between the total ionised mass and the maximum outflow rate for each AGN.

We plot these quantities in two different ways:

- 1) considering the total ionised mass only within the outflow range (Figure 11, left panel);
- 2) considering the ionised mass including the mass outside the outflow range (Figure 11, right panel).

When comparing the two plots, we find three AGNs, SDSS J115245.66+101623.8, 2MASX J13003807+5454367 and B2 1435+30, are separate from the remainder of the QSO2 sample. Their shift in positions from the left panel to the right panel on Figure 11 is due to their very extended [O III] emission, based on the ACS images, despite having very weak outflow rates.

To better understand the conditions under which the gas can be efficiently accelerated we can use the velocity calculation for radiatively driven outflows, discussed by Das et al. 2007, where:

$$v(r) = \sqrt{\int_{r_1}^r A_1 L_{bol} \frac{M}{r^2} - A_2 \frac{M(r)}{r^2} dr} \quad (13)$$

where M is the Force Multiplier, i.e., the ratio of the total absorption cross section to the Thomson cross section, and $M(r)$ is the enclosed mass at the distance r , determined from the radial mass distribution of the host galaxy, including the bulge. The constants A_1 and A_2 are given in Das et al. 2007.

Taking into account the relevant parameters in Equation 13, specifically, L_{bol} and $M(r)$, there are two possibilities that can explain the distinct characteristics of these three QSO2s:

- 1) The AGN was in a low state until recently. We can rule out the possibility that it was "off" completely by estimating the recombination times for the [O III] gas, as follows:

$$\tau = \frac{1}{n_H \alpha_{rec}} \quad (14)$$

The total recombination rate for $O^{++} - O^+$ is $\alpha_{rec} = 2.52 \times 10^{-12} \text{ cm}^3 \text{ sec}^{-1}$, at $10^4 K$ (Nahar 1999). Based on our model densities, the recombination times (Equation 14) are relatively short (the minimum recombination times are $\sim 3 - 4$ years and the maximum range from 245 years to 370 years), therefore, it is possible that the AGN could have turned completely off. However, even if the AGN was on, it appears to be in too weak of a state to accelerate the [O III] gas at these distances.

If the AGN was in a weak state, it could have enough ionising radiation to produce [O III]. However, the L_{bol} would have been too

Table 3. Numerical results for the mass and energetic quantities for the outflowing gas component in each target of our sample. All results account for the gas within the outflow region. Column 2 is the gas mass in units of $10^5 M_\odot$, Column 3 is peak mass outflow rate within the outflow region, Column 4 is the peak kinetic energy, Column 5 is the peak kinetic luminosity, Column 6 is the peak momentum, and Column 7 is the peak momentum flow rate for each QSO2. All listed values have a factor of ~ 4 uncertainty, as discussed in section 2.4.

Target	Total Mass ($10^5 M_\odot$)	Maximum \dot{M} (M_\odot/yr)	Maximum E (10^{53} ergs)	Maximum \dot{E} (10^{41} erg/s)	Maximum p (10^{46} dyne – s)	Maximum \dot{p} (10^{34} dyne)
(1)	(2)	(3)	(4)	(5)	(6)	(7)
SDSS J115245.66+101623.8	0.17	0.01	<0.01	<0.01	0.01	<0.01
MRK 477	152.0	3.55	1.34	0.75	2.09	0.3
MRK 34	337.0	10.3	26.20	12.80	9.15	2.83
2MASX J17135038+5729546	24.40	1.64	6.50	0.51	4.17	0.33
2MASX J16531506+2349431	2.54	0.34	2.23	0.25	0.95	0.10
2MASX J14054117+4026326	8.94	0.20	0.14	<0.01	0.34	0.01
2MASX J13003807+5454367	0.11	0.01	0.02	<0.01	0.02	<0.01
2MASX J11001238+0846157	25.60	0.63	1.32	0.07	1.68	0.06
2MASX J08025293+2552551	11.80	2.58	9.54	1.27	4.86	0.64
2MASX J07594101+5050245	4.44	0.14	0.29	0.07	0.15	0.03
FIRST J120041.4+314745	140.0	2.11	6.34	1.00	4.35	0.39
B2 1435+30	0.04	<0.01	0.45	<0.01	0.02	<0.01

Table 4. Deprojected distance from the nucleus for peak measurements of mass outflow rates (Column 2), kinetic luminosities (Column 3) and momentum flow rates (Column 4). Column 5 lists the highest deprojected outflow velocity at the maximum outflow rate position.

Target	Position of Peak \dot{M} (pc)	Position of Peak \dot{E} (pc)	Position of Peak \dot{p} (pc)	v_{out} at peak \dot{M} (km/s)
(1)	(2)	(3)	(4)	(5)
SDSS J115245.66+101623.8	70	70	70	70.9
MRK 477	310	80	310	22.9
MRK 34	1260	480	1320	341
2MASX J17135038+5729546	390	390	390	312
2MASX J16531506+2349431	260	260	260	498
2MASX J14054117+4026326	170	170	170	42.4
2MASX J13003807+5454367	50	50	50	206
2MASX J11001238+0846157	270	410	410	144
2MASX J08025293+2552551	480	480	480	393
2MASX J07594101+5050245	275	275	275	379
FIRST J120041.4+314745	525	840	525	325
B2 1435+30	100	100	100	518

low, up to recently, to accelerate the gas, that it would not be able to accelerate the gas, since the first term in Equation 13 becomes smaller compared to the gravitational deceleration term.

If we assume that the existence of outflows close to the AGN mean that the AGN is back to a high state, we can estimate how long ago it entered into this high state by using the size of the outflow regions and calculating the light crossing time for each target. Our calculations show that for SDSS J115245.66+101623.8, 2MASX J13003807+5454367 and B2 1435+30 these values are ~ 230 , 270 and 310 years ago, respectively.

2) The AGN has not varied in luminosity, but the three targets have different mass distributions than the other QSO2s in our sample. This possibility can be considered as two distinct cases:

a) The bulge mass is more centrally peaked. If this is the case, the second term in Equation 13 starts to dominate closer to the nucleus. However, the velocities and outflow rates for these three targets are similar to those of the rest of the sample in the same distance range (see Table 4). This suggests that this scenario is unlikely.

b) These objects possess a mass component which starts to dominate some distance from the AGN, as in Mrk 573 (see Fischer et al. 2017, figure 14). In this case, outflows can be generated close to the AGN, but, when this outer component starts to dominate, the gas cannot be accelerated. However, in order to explore this possibility,

we would need deeper (higher S/N) continuum images to derive the stellar mass profiles.

We are currently studying the dynamics of the outflows in these QSO2s, which will address this issue in more detail (Trindade Falcão et al. in preparation).

6 CONCLUSIONS

We use long-slit spectroscopy, [O III] imaging, and Cloudy photoionisation models to determine the mass outflow rates and energetics as functions of distance from the nucleus in a sample of twelve nearby ($z < 0.12$) luminous ($L_{bol} > 1.6 \times 10^{45}$ erg s $^{-1}$) QSO2s. Our results are as follows:

1. The outflows contain a total ionised gas mass ranging from $4.6^{+13.8}_{-3.4} \times 10^3 M_\odot$, for B2 1435+30, to $3.4^{+10.2}_{-2.5} \times 10^7 M_\odot$, for Mrk 34, with a total kinetic energy varying between $8.9^{+26.7}_{-6.7} \times 10^{50}$ ergs, for SDSS J115245.66+101623.8, and $2.9^{+9.0}_{-2.2} \times 10^{55}$ ergs, for Mrk 34.

2. F2018 found that the outflows extend to a maximum of 1,600 pc. Our results show that these outflows reach a peak outflow rate ranging from $\dot{M}_{out}(r) = 9.3^{+27.9}_{-7.0} \times 10^{-3} M_\odot \text{ yr}^{-1}$, for B2 1435+30, to $10.3^{+30.9}_{-7.7} M_\odot \text{ yr}^{-1}$, for Mrk 34, at distances between 100 pc and 1260 pc from the SMBH.

3. The maximum kinetic luminosity of the outflow ranges from $3.4^{+10.2}_{-2.5} \times 10^{-8}$ of the AGN bolometric luminosity for SDSS J115245.66+101623.8 to $4.9^{+14.7}_{-3.7} \times 10^{-4}$ of the AGN bolometric luminosity for Mrk 34⁸. The large range in kinetic luminosity compared to the narrow range in L_{bol} (see Table 2) is in contrast to the correlation between the kinetic luminosity and L_{bol} suggested by Fiore et al. (2017). Our results indicate that the [O III] winds are not an efficient feedback mechanism, based on the criteria of Di Matteo et al. (2005) and Hopkins & Elvis (2010). This means that, not only do the outflows not extend far enough to clear the bulge of gas (F2018), they also lack the power to do so.

4. As noted above, Mrk 34 is the target in our sample that shows the highest outflow rate and most extended outflows. We calculate what the outflow rates would have had to have been in order to reach the minimum value required for efficient feedback. We find that Mrk 34 would have to have, at its position of maximum \dot{E} , an outflow rate of $20 M_{\odot} \text{ yr}^{-1}$, corresponding to a mass of $8.2 \times 10^5 M_{\odot}$ at that position. This value is 10 times greater than our measured outflow rate at that same position. We also find that the required mass for efficient feedback is ~ 0.01 times the amount for a covering factor of unity.

These calculations show that this object could potentially, at these velocities, make efficient outflows, but such energetic outflows are not detected. One possibility is that the lack of [O III] gas is the result of rapid thermal expansion, with the result that its ionisation state increases to the point where it becomes X-ray emitting gas. In fact, *Chandra* imaging of Mrk 34 has revealed X-ray emission line gas extending the size of the [O III] emission line region (Fischer et al. in preparation). We are currently exploring this possibility (Trindade Falcão et al. in preparation). Also, neutral and molecular gas could be contributing to the outflow (see section 2.5) and, altogether, could provide a much higher mass outflow rate (Tombesi et al. 2015; Bischetti et al. 2019).

5. Three of the targets in our sample show very extended [O III] emission, but weak outflow rates. Based on their compact outflow regions, but extended [O III] emission, we study two different scenarios: these AGNs were in a very low state until recently, but have entered a high state, during which they are able to accelerate outflows. Or these AGNs could be housed in more massive host galaxies, prohibiting successful radiative driving at distances greater than a few hundred parsecs.

Based on these results, we do not see the outflows traced by [O III]-emission-line gas being powerful enough to generate efficient feedback. However, the presence of disturbed gas at larger radial distances (F2018), suggests that the AGN have an effect outside the outflow regions. One possibility is that this is the result of X-ray winds, which may form from thermal expansion of the [O III] gas (Fischer et al. 2019; Kraemer et al. 2020). We are currently exploring this scenario (Trindade Falcão et al., in preparation).

ACKNOWLEDGEMENTS

The authors thank the anonymous referee for helpful comments that improved the clarity of this paper. Support for this work was provided by NASA through grant number HST-GO-13728.001-A from

the Space Telescope Science Institute, which is operated by AURA, Inc., under NASA contract NAS 5-26555. Basic research at the Naval Research Laboratory is funded by 6.1 base funding. T.C.F. was supported by an appointment to the NASA Postdoctoral Program at the NASA Goddard Space Flight Center, administered by the Universities Space Research Association under contract with NASA. T.S.-B. acknowledges support from the Brazilian institutions CNPq (Conselho Nacional de Desenvolvimento Científico e Tecnológico) and FAPERGS (Fundação de Amparo à Pesquisa do Estado do Rio Grande do Sul). L.C.H. was supported by the National Key R&D Program of China (2016YFA0400702) and the National Science Foundation of China (11473002, 11721303). M.V. gratefully acknowledges financial support from the Danish Council for Independent Research via grant no. DFF 4002-00275 and 8021-00130.

This research has made use of the NASA/IPAC Extragalactic Database (NED), which is operated by the Jet Propulsion Laboratory, California Institute of Technology, under contract with the National Aeronautics and Space Administration. This paper used the photoionization code Cloudy, which can be obtained from <http://www.nublado.org>. We thank Gary Ferland and associates, for the maintenance and development of Cloudy.

DATA AVAILABILITY

Based on observations made with the NASA/ESA Hubble Space Telescope, and available from the Hubble Legacy Archive, which is a collaboration between the Space Telescope Science Institute (STScI/NASA), the Space Telescope European Coordinating Facility (ST-ECF/ESAC/ESA) and the Canadian Astronomy Data Centre (CADC/NRC/CSA).

REFERENCES

- Ahumada R., Prieto C. A., Almeida A., Anders F., Anderson S. F., Andrews B. H., Anguiano B., 2019, arXiv:1912.02905
- Antonucci R., 1993, ARA&A, 31, 473
- Bae H.-J., Woo J.-H., 2016, ApJ, 828, 97
- Baron D., Netzer H., 2019, MNRAS, 482, 3915
- Begelman M. C., 2004, Carnegie Observatories Astrophysics Series, 1, 374
- Bischetti M., et al., 2019, A&A, 628, A118
- Buchner J., et al., 2014, A&A, 564, A125
- Cardelli J. A., Clayton G. C., Mathis J. S., 1989, ApJ, 345, 245
- Collins N. R., Kraemer S. B., Crenshaw D. M., Ruiz J., Deo R., Bruhweiler F. C., 2005, ApJ, 619, 116
- Costa T., Sijacki D., Haehnelt M. G., 2014, MNRAS, 444, 2355
- Crenshaw D. M., Kraemer S. B., 2005, ApJ, 625, 680
- Crenshaw D. M., Kraemer S. B., 2012, ApJ, 753, 75
- Crenshaw D. M., Kraemer S. B., George I. M., 2003, ARA&A, 41, 117
- Crenshaw D. M., Kraemer S. B., Schmitt H. R., Jaffé Y. L., Deo R. P., Collins N. R., Fischer T. C., 2010, AJ, 139, 871
- Crenshaw D. M., Fischer T. C., Kraemer S. B., Schmitt H. R., 2015, ApJ, 799, 83
- Das V., Crenshaw D. M., Kraemer S. B., 2007, ApJ, 656, 699
- Davies R., et al., 2020, MNRAS, arXiv:2003.06153
- Di Matteo T., Springel V., Hernquist L., 2005, Nature, 433, 604
- Dietrich M., Hamann F., Shields J. C., Constantin A., Heidt J., Jäger K., Vestergaard M., Wagner S. J., 2003, ApJ, 589, 722
- Dong X., Wang T., Wang J., Yuan W., Zhou H., Dai H., Zhang K., 2008, MNRAS, 383, 581
- Duras F., et al., 2020, A&A, 636, A73
- Ferland G. J., et al., 2017, Rev. Mex. Astron. Astrofis., 49, 1379
- Feroz F., Hobson M. P., 2008, MNRAS, 384, 449
- Feroz F., Hobson M. P., Bridges M., 2009, MNRAS, 398, 1601

⁸ Our maximum kinetic luminosity value for Mrk 34 is about a factor of 10 less than that computed by Revalski et al. (2018). The discrepancy is due to the presence of a high mass/low density component, which was not included in our analysis.

- Feroz F., Hobson M. P., Cameron E., Pettitt A. N., 2013, *The Open Journal of Astrophysics*
- Fiore F., et al., 2017, *A&A*, 601, A143
- Fischer T. C., Crenshaw D. M., Kraemer S. B., Schmitt H. R., 2013, *ApJ*, 209, 1
- Fischer T. C., Crenshaw D. M., Kraemer S. B., Schmitt H. R., Turner T. J., 2014, *ApJ*, 785, 25
- Fischer T. C., et al., 2017, *ApJ*, 834, 30
- Fischer T. C., et al., 2018, *ApJ*, 856, 102
- Fischer T. C., et al., 2019, *ApJ*, 887, 200
- Gandhi P., et al., 2014, *ApJ*, 792, 117
- Ganguly R., Brotherton M. S., 2008, *ApJ*, 672, 102
- Genzel R., Förster Schreiber N. M., Rosario D., Lang P., et al. 2014, *ApJ*, 796, 7
- Greene J. E., Zakamska N. L., Ho L. C., Barth A. J., 2011, *ApJ*, 732, 9
- Groves B. A., Dopita M. A., Sutherland R. S., 2004, *A&AS*, 153, 9
- Hamann F., Ferland G., 1998, *ARA&A*, 37, 487
- Harrison C. M., Alexander D. M., Mullaney J. R., Swinbank A. M., 2014, *MNRAS*, 441, 3306
- Heckman T. M., Kauffmann G., Brinchmann J., Charlot S., Tremonti C., White S. D. M., 2004, *ApJ*, 613, 109
- Hopkins P. F., Elvis M., 2010, *MNRAS*, 401, 7
- Joye W. A., Mandel E., 2003, in *Astronomical Data Analysis Software and Systems XII. Astronomic Society of the Pacific*, p. 489
- King A., Pounds K., 2015, *ARA&A*, 53, 115
- Kormendy J., Ho L. C., 2013, *ARA&A*, 51, 511
- Kraemer S. B., Harrington J. P., 1986, *ApJ*, 307, 478
- Kraemer S. B., Ruiz J. R., Crenshaw D. M., 1998, *ApJ*, 508, 232
- Kraemer S. B., Crenshaw D. M., Hutchings J. B., Gull T. R., Kaiser M. E., Nelson C. H., Weistrop D., 2000, *ApJ*, 531, 278
- Kraemer S. B., et al., 2001, *ApJ*, 551, 671
- Kraemer S., Crenshaw D. M., George I. M., Netzer H., Turner T. J., Gabel J. R., 2002, *ApJ*, 577, 98
- Kraemer S. B., et al., 2012, *ApJ*, 751, 84
- Kraemer S. B., Turner T. J., Couto J. D., Crenshaw D. M., Schmitt H. R., Revalski M., Fischer T. C., 2020, *MNRAS*, 493, 3893
- Lamastra A., Bianchi S., Matt G., Perola G. C., Barcons X., Carrera F. J., 2009, *A&A*, 504, 73
- Laor A., Fiore F., Elvis M., Wilkes B. J., McDowell J. C., 1997, *ApJ*, 477, 93
- Liu G., Zakamska N. L., Greene J. E., Nesvadba N. P. H., Liu X., 2013, *ApJ*, 436, 2576
- Mahoro A., Pović M., Nkundabakura P., 2017, *MNRAS*, 471, 3226
- McElroy R., Croom S. M., Pracy M., Sharp R., Ho I.-T., Medling A. M., 2015, *MNRAS*, 446, 2186
- Meléndez M., Kraemer S. B., Weaver K. A., Mushotzky R. F., 2011, *ApJ*, 738, 6
- Mullaney J. R., Alexander D. M., Fine S., Goulding A. D., Harrison C. M., C. H. R., 2013, *MNRAS*, 433, 622
- Müller-Sánchez F., Prieto M. A., Hicks E. K. S., Vives-Arias H., Davies R. I., Malkan M., Tacconi L. J., Genzel R., 2011, *ApJ*, 739, 69
- Nagao T., Murayama T., Taniguchi Y., 2001, *ApJ*, 546, 744
- Nagao T., Murayama T., Shioya Y., Taniguchi Y., 2002, *ApJ*, 575, 721
- Nahar S. N., 1999, *ApJS*, 120, 131
- Netzer H., 2009, *MNRAS*, 399, 1907
- Netzer H., Chelouche D., George I. M., Turner T. J., Crenshaw D. M., Kraemer S., Nandra K., 2002, *ApJ*, 571, 256
- Nevin R., Comerford J., Müller-Sánchez F., Barrows R., Cooper M., 2016, *ApJ*, 832, 67
- Osterbrock D. E., Ferland G. J., 2006, *Astrophysics of gaseous nebulae and active galactic nuclei*, 2 edn. University Science Books, Sausalito, CA
- Peterson B. M., 1997, *An introduction to active galactic nuclei*, xvi edn. Cambridge, New York Cambridge University Press
- Rafter S. E., Crenshaw D. M., Wiita P. J., 2009, *AJ*, 137, 42
- Revalski M., et al., 2018, *ApJ*, 867, 88
- Reyes R., et al., 2008, *AJ*, 136, 2373
- Ryon J. E. e. a., 2019, *ACS Instrument Handbook*, version 18.0 edn. STScI, Baltimore
- Savage B. D., Mathis J. S., 1979, *ARA&A*, 17, 73
- Seaton M. J., 1979, *MNRAS*, 187, 73
- Silk J., 2013, *ApJ*, 722, 112
- Snow T. P., Witt A. N., 1996, *ApJ*, 468, L65
- Storchi-Bergmann T., Schnorr-Muller A., 2019, *Nature Astronomy*, 3, 48
- Storchi-Bergmann T., Rodríguez-Ardila A., Schmitt H. R., 1996, *AJ*, 472, 83
- Storchi-Bergmann T., Schmitt H. R., Calzetti D., Kinney A. L., 1998, *AJ*, 115, 909
- Talbot R. J. J., Arnett W. D., 1973, *ApJ*, 186, 51
- Tombesi F., Meléndez M., Veilleux S., Reeves J. N., González-Alfonso E., Reynolds C. S., 2015, *Nature*, 519, 436
- Veilleux S., Cecil G., Bland-Hawthorn J., 2005, *ARA&A*, 43, 769
- Woo J.-H., Bae H.-J., Son D., Karouzos M., 2016, *ApJ*, 817, 108
- Woodgate B. E., Kimble R. A., Bowers C. W., Kraemer S., Kaiser M. E., Danks A. C., Grady J. F., Loiacono J. J., 1998, *ASP Conf. Ser.*, 110, 1183
- Wylezalek D., Morganti R., 2018, *Nature Astronomy*, 2, 181
- Wylezalek D., Zakamska N. L., 2016, *MNRAS*, 461, 3724
- Zubovas K., Bourne M. A., 2017, *MNRAS*, 468, 4956
- Zubovas K., King A., 2012, in *AGN Winds in Charleston. Astronomic Society of the Pacific Series*, Charleston, South Carolina, p. 235

This paper has been typeset from a \LaTeX file prepared by the author.